


Article

Design and Analysis: Servo-Tube-Powered Liquid Jet Injector for Drug Delivery Applications

Rocco Portaro and Hoi Dick Ng * 

Department of Mechanical, Industrial and Aerospace Engineering, Concordia University,
Montreal, QC H3G 1M8, Canada; portaro_154@hotmail.com

* Correspondence: hoing@encs.concordia.ca

Abstract: The current state of commercially available needle-free liquid jet injectors for drug delivery offers no way of controlling the output pressure of the device in real time, as the driving mechanism for these injectors provides a fixed delivery pressure profile. In order to improve the delivery efficiency as well as the precision of the targeted tissue depth, it is necessary to develop a power source that can accurately control the plunger velocity. The duration of a liquid jet injection can vary from 10 to 100 ms, and it generate acceleration greater than 2 g (where g is the gravity); thus, a platform for real-time control must exhibit a response time greater than 1 kHz and good accuracy. Improving the pioneering work by Taberner and others whereby a Lorentz force actuator based upon a voice coil is designed, this study presents a prototype injector system with greater controllability based on the use of a fully closed-loop control system and a classical three-phase linear motor consisting of three fixed coils and multiple permanent magnets. Apart from being capable of generating jets with a required stagnation pressure of 15–16 MPa for skin penetration and liquid injection, as well as reproducing typical injection dynamics using commercially available injectors, the novelty of this proposed platform is that it is proven to be capable of shaping the real-time jet injection pressure profile, including pulsed injection, so that it can later be tailored for more efficient drug delivery.



Citation: Portaro, R.; Ng, H.D.

Design and Analysis:

Servo-Tube-Powered Liquid Jet

Injector for Drug Delivery

Applications. *Appl. Sci.* **2022**, *12*, 6920.

[https://doi.org/10.3390/](https://doi.org/10.3390/app12146920)

[app12146920](https://doi.org/10.3390/app12146920)

Academic Editor: Francesca

Scargiali

Received: 15 June 2022

Accepted: 5 July 2022

Published: 8 July 2022

Publisher's Note: MDPI stays neutral with regard to jurisdictional claims in published maps and institutional affiliations.



Copyright: © 2022 by the authors. Licensee MDPI, Basel, Switzerland. This article is an open access article distributed under the terms and conditions of the Creative Commons Attribution (CC BY) license (<https://creativecommons.org/licenses/by/4.0/>).

Keywords: needle-free injection technology; liquid jet injection; drug delivery; linear servo actuator

1. Introduction

Today's society has witnessed tremendous technological breakthroughs that are helping to deal with the challenges posed by an ever-increasing population and other global events, such as novel viruses, e.g., COVID-19. Thus, a great emphasis is placed on providing the most efficient and comfortable health care to patients. In order to achieve this objective, the health care profession often implements engineering concepts to solve the problems it faces. Surgical methods, such as minimally invasive robotic surgery, and medical imaging techniques, such as magnetic resonance imaging and computed tomography scans, are just a few examples of biomedical engineering advances in the past few decades that make medical diagnostics and procedures safer and more effective and decrease recovery time. One technology that has yet to be fully exploited in the realm of biomedical engineering is that of micro-sized, high-speed liquid jets. These micro-sized jets demonstrate great promise for their use in needle-free drug delivery, as well as mass immunization [1]. This can greatly aid in vaccination efforts when health care professionals are faced with the task of rapidly delivering an extremely large number of injections, reducing biohazardous waste, delivering medication more efficiently at targeted skin locations and decreasing the reluctance to undergo vaccination due to needle stick phobias (trypanophobia). The engineering design goals are to advance this technology for large volume injection with good controllability and delivery precision. This would require a thorough understanding of the relationship between liquid jet dynamics and injector parameters, as well as efficient controlled release mechanisms, in order to improve the delivery efficiencies and performance of the liquid jet injection system.

The production of needle-free liquid jet injections is accomplished by a high-speed jet created using a power source; the jet carries enough energy to puncture human skin and deliver a precise volume of medication within a specific target [2,3]. In commercially available injectors, a power source compresses a piston, which in turn forces a column of fluid through a micro-orifice on the order of 50 to 250 μm in diameter. The resulting compression of the fluid column creates a high-speed jet with speeds on the order of 100–200 m/s and Reynolds numbers in excess of 100,000. Typically, the pressure increase in the fluid column can peak at more than 30 MPa within 0.5 ms. These pressure values are well above the minimum threshold of 3–15 MPa for fracturing skin. In fact, commercially available injectors that are capable of producing such pressure peaks can routinely deliver 0.1 to 1 mL of fluid at depths greater than 10 mm. For summary, a number of recent review articles on this technology and its state-of-the-art can be found in the literature, e.g., [1–8].

The power source driving an injection remains one of the most influential and researched aspects of liquid jet injectors. It is important to note that, although the compression of a fluid column to create a high-speed jet is common throughout various types of injectors, the power sources driving the injection vary greatly. Early needle-free injectors were spring-powered, e.g., [9–19]; driving the injection was accomplished by compressing a spring that is subsequently released to drive a plunger that forces fluid through an orifice. In these types of injectors, spring compression was achieved using screw mechanisms or bulky levers. Spring-powered injectors provide a very cost-effective means of delivering injection because the spring powering the injection can usually last for the life of the injector.

Although spring-powered injectors are simple in construction and have an inexhaustible power source, they exhibit several problems. One of the major drawbacks deals with variable injection depth. Experimentation is often required in order to attain a target tissue region. This is due to the nature of the device; when the spring is released from its compressed state, the energy decreases nonlinearly. Thus, the highest forces are produced at the start of the injection, which is necessary to breach the epidermis; however, the subsequent jet power decays exponentially.

The advent of gas-powered needle-free injectors, e.g., [20–27], has helped deliver medication to target areas of the skin more accurately. These injectors contain a highly pressurized cartridge of inert gas (normally not higher than 8 bars), usually helium or carbon dioxide, that propels a piston. The piston is locked in place by a trigger mechanism, and when the piston is released, it compresses a column of fluid that is then forced through an orifice to create a liquid jet. Gas-powered injectors exhibit greater stability throughout injection delivery due to a more constant application of force on the driving piston. The pressure decay in the compressed gas cartridge is negligible during a typical injection, which is on the order of 100 ms [25]. Although there is still a pressure peak during the first few milliseconds of injection followed by an average injection pressure, the average injection pressure can be maintained at a specified level and does not decay as rapidly as spring-powered injectors. This makes it possible to target specific areas more easily, as well as giving gas-powered injectors the ability to target deep subcutaneous tissues. Recently, a similar, alternative injector design was also proposed using a hydro-pneumatic mechanism [28].

Although both gas-powered and spring-powered injectors form the majority of power sources available in commercial injectors, these types of power sources lack controllability. This implies that, once they begin to drive the injection, there is no means of modifying the application of power such that variable factors, such as friction and fluid damping, can be considered. Thus, the stagnation pressure profile produced by the injectors is fixed from its design stages and cannot be modified. Furthermore, because the power application is limited with these types of injectors, it is necessary to couple the orifice diameter with the total volume of liquid to be delivered. This usually results in the use of larger jet diameters to limit the time duration of the injection. The use of larger-diameter jets causes pain, bruising and hematomas, which are among the primary reasons that have limited the widespread use of liquid jet injectors.

In order to overcome the aforementioned limitations and improve the controllability of liquid jet injection, it is necessary to precisely control the pressure profile exhibited by the liquid jet. Among more recently proposed concepts to drive needle-free liquid injectors, such as: the use of a single piezoelectric crystal [29] or a piezoelectric crystal stack [30] to actuate a piston, expansion of vapor bubbles using laser radiation [31–37], electrical current discharge [38], and pyrotechnics [39], it seems that electronic linear actuators provide one of the most practical and efficient methods for complete closed-loop control of liquid jet production. They offer real-time control and do not require high voltages or subject the fluid to electric charges or laser radiation as in other experimental techniques. This technology has been applied to an experimental device proposed by [40] and was subsequently used in many studies, e.g., [41–45], and in commercialization [46,47], whereby a Lorentz force actuator based upon a voice coil was used to compress a column of fluid, using a plunger traveling at a specified velocity profile. The results of this study illustrated that a semi-closed-loop system consisting of a simple coil/one magnet actuator coupled to a linear variable differential transformer (LVDT) could successfully be used to dynamically shape a specific pressure profile. Although the system produced controllable traces, there is a lack of information on its precision.

The design of the Lorentz force actuators used in these studies is based on simple voice coils, which have some significant drawbacks. This is revealed by examining the fundamental principles governing the force output of these actuators. In its simplest form, a voice coil can be considered a non-commutated DC motor, having one winding and one permanent magnet. In the case of the linear actuator utilized by Taberner et al. [40], the permanent magnet is chosen as the stationary component, with the coil providing motion. The force output is prescribed by $F = B \times i$, where F is the force (N), B is the magnetic field flux (T) and i is the current (A) flowing through the coil. The magnetic field produced by the magnets permeates an air gap and is orthogonal to the coil, and thus produces a force that is prescribed by the cross-product of the magnetic field flux and the current energizing the coil.

In an ideal scenario, the motor constant should exhibit an independent relationship between current, speed, position and temperature. However, because of the inherent construction of this type of motor, whereby only one coil can be energized, the velocity and force of the plunger on this type of actuator are dependent on the amount of current that is passed through the coil. This means that an increase in force will be accompanied by a proportional response in the speed of the plunger. When voltage is applied to the coil, the magnetic flux forces the coil to move in the direction normal to current flow. This motion will occur so long as the coil is energized. In order to provide precise motion, a control loop is created through the use of a simple LVDT, which returns the plunger's position as a function of time. The feedback from the LVDT is used in conjunction with a PID loop controlling both the magnitude and polarity of the voltage sent through the coil, ensuring that the proper plunger position is accomplished. The control loop must exhibit a relatively high-frequency response rate in order to ensure the plunger is following the proper trajectory, given that injections take place within milliseconds and the stroke of the plunger can be on the order of several centimeters depending on the volume of liquid delivered.

However, when precise velocity control is required and the voice coil encounters higher forces due to the coupling between force and velocity, it becomes difficult for the control loop to follow the proper trajectory. This is a very important notion as the health care industry moves towards adopting newer technologies, such as DNA therapy [48,49]; with more viscous formulations and larger injection volumes, the energy output for needle-free injectors will grow. Although voice coils exhibit very good high-speed response, increasing power output becomes difficult. Power output can be increased by increasing either the current or the magnetic field flux. This is usually accomplished by using more powerful and larger magnets, applying more current, which entails using larger coils, or diminishing the air gap between the magnet/coil. It should also be noted that optimizing a voice coil motor


for power will inevitably affect the response times of the system, as larger magnets/coil assemblies represent larger moving masses of greater inertia. Furthermore, Ruddy et al. [43] found that the coupling between voice coil stroke, size and efficiency interacts with the mechanics of pressurizing a fluid in a piston–cylinder apparatus to give a scaling law. For a given input power, the required voice coil mass grows faster than the injection volume, with $M \propto V^{6/5}$. As a result, hand-held injectors delivering volumes of over 0.5 mL are not practical using voice coil actuation. Moreover, the voice coil design does not lend itself well to large travels, meaning that providing repeated large-volume injections as required by mass vaccination in the animal health industry would not be feasible.

In order to improve on the shortcoming of voice coil motors and to provide a platform with greater controllability, it is necessary to use a linear actuator with a slightly different topology. This study will examine the use of a classical three-phase linear motor consisting of three fixed coils and multiple permanent magnets. Each coil is controlled individually, i.e., commutated with respect to the permanent magnets. It should be noted that studies that examine this motor design have been conducted concurrently with the development of this prototype [50]. The studies conducted by Do et al. [51,52] illustrate the optimization procedures for sizing a permanent magnet synchronous motor used for liquid jet delivery and test a custom-built motor in an open-loop configuration without current control. In this study, a prototype that utilizes a commercially available linear motor with well-established motor constants and parameters, as well as modern power electronics to provide true closed-loop control, is constructed. This prototype is then tested for its ability to reproduce specific plunger velocity profiles whilst compensating for factors that influence plunger motion via a PID loop. This will yield an accurate portrayal of the ability for linear permanent magnet motors to shape the pressure output of liquid jet injections.

The motor chosen for the construction of a prototype injector was provided by Dunkermotoren GmbH, and the specifications of this motor are outlined in the following Table 1:

Table 1. Dunkermotoren GmbH STA-2508 Linear Servo Tube Specifications (2022) <https://www.dunkermotoren.com/>, (accessed on 1 May 2022).

Specification	Value
Peak Force	624 N
Peak Current	20 A
Force Constant (Sinusoidal-Comm)	44.1 N/Arms
Pole Pitch	51.2 mm
Peak Velocity	4.7 m/s



In this actuator, magnets are enclosed within a circular actuator tube. The effective travel of this device can be increased or decreased as desired by lengthening the actuator tube. The core of the proposed actuator has two main components: a moving actuator rod and a fixed stator housing. The actuator rod consists of a non-magnetic stainless-steel tube filled with 13 high-quality, 25 mm circular neodymium NdFeB magnets. The actuator rod sits in a polymer (PTFE) bearing placed within the stator housing, which is encapsulated by a series of three windings that enable the actuator rod to be commutated. The process of commutation is an important attribute; despite adding an extra level of complexity, it aids in decoupling the relationship between the force output of the device and the velocity of the plunger. This means that, for a fixed velocity, the amount of force applied to the plunger can vary independently by increasing or decreasing the different phase currents. The process of commutation maintains an orthogonal relationship between the magnetic fields in order to maximize force output [53].

The actuator chosen for this study is equipped with three Hall effects sensors as well as a sinusoidal encoder. The Hall effects sensors determine the relationship of the magnetic field flux of the permanent magnets within the actuator tube upon motor start-up, and

the sinusoidal encoder is then used to vary the phase angle as a function of actuator tube displacement, knowing the fixed pole pitch of the magnets.

Commutation of the coils and precise actuator motion are accomplished via an inverter/amplifier servo drive. In this study, the Parker Compax3 Servo Drive (Parker Hannifin Corporation, Cleveland, OH, USA) was utilized due to its ability to accurately drive linear motors; see Table 2 for its specifications. This unit converts an AC waveform into a DC square wave. AC current is converted to DC using a bridge rectifier, and the DC current is then fed to six internal gate bridge rectifiers (IGBTs), which act as high-speed switches. The switching of the IGBTs is controlled via a microcontroller within the drive at a maximum frequency of 16 kHz and utilizes a space vector modulation (SPVM) algorithm in order to obtain a three-phase AC waveform with the desired amplitude and frequency. The microcontroller also receives a desired motion profile, and the feedback from the sinusoidal encoder in conjunction with a PID loop will ensure the required motion ensues.

Table 2. Parker Compax3 T10 Drive Specifications (Parker Hannifin Corp. parkermotion.com, accessed on 1 May 2022).

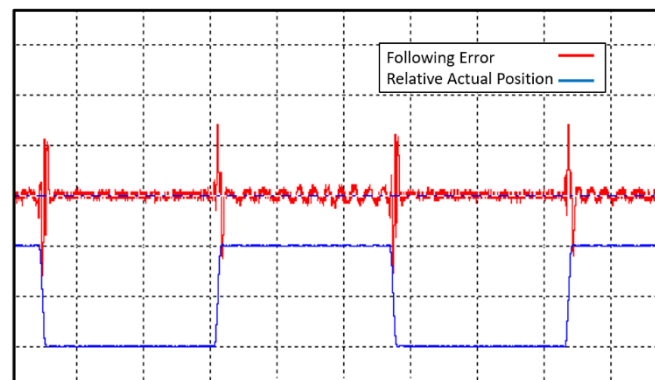
Specification	Value
Power Input	253 V.AC @ 60 Hz/50 Hz
Input Phases	3 \emptyset
PWM Switching	16 kHz
Continuous Current Output (RMS)	15 amps
Peak Current Output (RMS)	30 amps
Commutation	Sinusoidal
Velocity Loop	125 μ s
Position Loop	125 μ s

In this study, the Compax3 is used in position control mode, whereby a finite series of pulses are sent to the drive at a predetermined frequency. The pulse train sent to the drive must adhere to industrial standards and therefore have a maximum amplitude of 24 volts, with a maximum frequency of 500 kHz. The drive then utilizes an internal map to correlate each rising edge of a pulse with a fixed linear distance of the actuator rod's pole pitch. The sinusoidal encoder provides real-time feedback of the actuator rod's displacement, and a PID loop ensures that motor windings are energized appropriately to compensate for any following error (Parker Hannifin Corp. 2013). The exact values of the parameters used in the PID loop were established after consultation with Dunkermotoren and optimized experimentally. This was accomplished using software provided by Parker (C3 servo Manager), whereby the system was tested under experimental load and optimized to decrease following error whilst maintaining stability of the PID loop.

The parameters depicted in Table 3 represent the final tuning of the actuator. Tuning was performed by applying an oscillatory step response to the system at a speed of 4 m/s and a distance of 20 mm and then utilizing an oscilloscope to track the actual position, commanded position and following error versus time. The PID parameters were modified until minimal overshoot, minimal following error and good vibration suppression about the target destination were achieved. Figure 1 below demonstrates both the actual position and the following error. The time division on the horizontal axis is set to 400 ms, and the divisions for the error and position are 5 increments and 1000 increments, respectively. As is normal with a step response input to a PID loop, a maximum deviation of 8 increments (80 μ m) is observed; when the relative motion is commanded, the plunger deviates from its real-time target, but the error is recuperated in a timely manner. The tuning performed on the PID ensures that, when the actuator is coupled to the injector head, the plunger will follow its outlined trajectory with ± 20 increments, irrespective of the changing factors, such as friction, nozzle size or fluid viscosity. This will greatly simplify modeling the output pressure of the device, as the only relationship that needs to be considered is that of the pressure increase in the injection chamber as a function of plunger displacement.

Table 3. PID Loop Relevant Parameters.

Specification	Value
Pulses Per	1000 cm
Permissible Deviation	20 increments
Actuator Rod Weight	1.310 kg
Stiffness Gain	200%
Damping Gain	40%
Mass Inertia Gain	60%
Velocity Feed Forward Gain	100%
Acceleration Feed Forward Gain	100%
Current Feed Forward Gain	100%
Tracking Error Filter	50 μ s

**Figure 1.** Following error as a function of displacement.

The objective of this study is to design and manufacture a prototype liquid jet injector that can provide a platform capable of shaping the real-time jet injection pressure profile to adapt to different drug delivery needs. Using the servo-tube technology introduced above and a full loop control strategy, this paper serves to highlight how the proposed servo-driven injector could exhibit accurate real-time control of the jet stagnation pressure, as well as provide enough power to penetrate human tissue. In addition to the ability to produce large-volume, viscous injections, the proposed platform has the ability to dynamically react to external variables, such as friction, fluid viscosity, nozzle size and temperature deviations, without the need to rely on mathematical models to predict the device's output, but rather by compensating for them using a control loop.

2. Materials and Methods

2.1. Prototype Device Specification

In order to produce the required liquid jets for experimental analysis, an injection chamber, a small-diameter plunger and a nozzle must be added to the actuator. The injection chamber is fitted to the servo actuator by utilizing an adapter block that mounts directly to one of the stator's end caps. This ensures concentricity between the actuator and the injection chamber. Furthermore, in this manner, the device can be used for future works, and different injection chamber geometries can be studied and verified for performance. The prototype consists of an injection chamber with a 6.35 mm bore that is terminated by a thread that receives a nozzle. The orifice-type nozzles manufactured by O'Keefe used in this experimental device have successfully been used in previous studies [25,54] to obtain confined jets with minimal divergence. This study will evaluate the performance of the device in shaping pressure profiles utilizing four different nozzles outlined in Table 4.

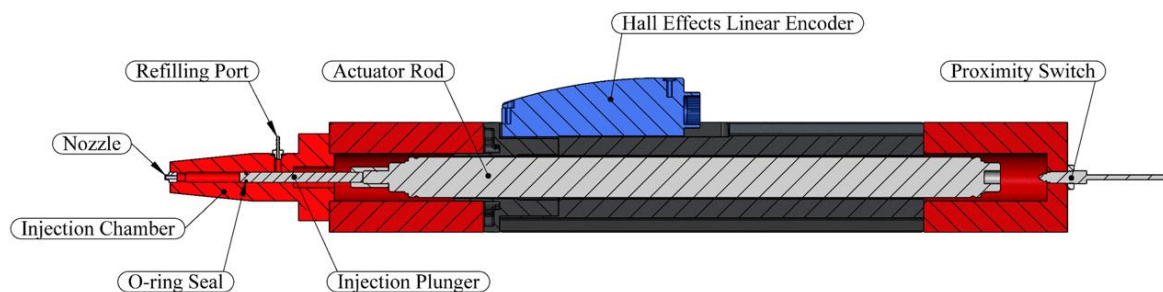
Table 4. Nozzle specification.

Nozzle Number	Orifice Diameter (μm)
6	150
8	200
10	250
12	300

The injection chamber also contains one threaded port, which serves as a filler inlet, in order to recharge the chamber with fluid. The injection chamber also houses a plunger with an O-ring sealed tip, see details in Table 5. It is important to note that, when the plunger is clear of the filling port, the size of the bore is increased to allow air to vent as the chamber is filled. The plunger is coupled to the actuator rod through a threaded coupling. The stator end cap on the opposing side of the injection chamber is capped by a block containing an OMRON D5A limit switch capable of 3 μm precision. The limit switch will enable the precise referencing of a home position, from which absolute measurements can be applied. Figure 2 illustrates how these individual components are coupled together to produce the injector.

Table 5. Servo-Tube Injector Specifications.

Specification	Value
Injection Chamber Diameter	6.35 mm
Injection Chamber Volume	2.5 mL
O ring-Seal	1/8 \times 1/4 \times 1/16 – 75 duro

**Figure 2.** Schematic of complete servo-tube-driven injector.

In order to accurately gather pressure traces, the experimental prototype is fitted to a specially designed stand, as shown in Figure 3. This stand makes it possible to mount the injector in a vertical position and provides fine positioning of the injector height so that the standoff distance can be adjusted and accurately maintained upon subsequent runs. The stand weighs 75 kg and is constructed from a 12.7 mm thick plate; this provides the necessary stability to cope with the forces generated by the servo-tube actuator.

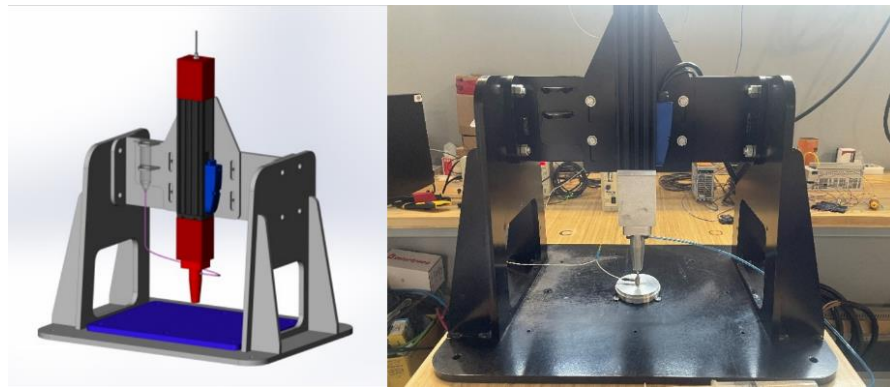


Figure 3. Test stand for servo-driven injector.

2.2. Actuator Motion

In order for the actuator to deliver an injection, a motion profile is required as shown in Figure 4. As previously mentioned, this must be produced in the form of a pulse stream. The pulse stream specifies the physical distance that the plunger will move downward, as well as its velocity. This is controlled by the number of pulses and the rising-edge-to-rising-edge frequency.



Figure 4. Block diagram of semi-closed-loop servo-tube injector.

In this study, a field-programmable gate array (FPGA), specifically a Xilinx ZYNQ SoC, is used to construct a stream of varying-frequency TTL pulses with an amplitude of 0 to 5 V. This device contains thousands of logic gates as well as many RAM blocks that can be configured through the use of hardware descriptive language (HDL) in order to create complex digital circuits. In the case of this experiment, an NC oscillator is developed, which outputs pulses based on a velocity lookup table; the system runs on a 100 MHz clock, which allows pulsing frequencies of up to 50 MHz to be generated. The FPGA is mounted on a development board provided by AVNET, which makes it possible to program the FPGA chip and gain access to all inputs and outputs via breakout connectors. The TTL (0–5 V) pulse stream must then be converted through the use of a high-speed opto-coupler into a 24 V pulse stream; a Weidmuller Opto-coupler providing a push–pull output and capable of 600 kHz switching frequencies is used for this task. Figure 5 shows the setup outputting a pulse stream of 35 kHz correlating to (0.35 m/s) produced at 24 V, with the addition of a 1 k ohm pull-up resistor between the 24 V and the digital pulse input of the servo amplifier.

The pulse stream does not exhibit acceleration or deceleration, as the servo amplifier has a built-in function that automatically counts the number of increments and input frequency and then applies trapezoidal trajectory planning, whereby the increments/ s^2 (accel/decel) and increments/ s^3 (jerk) can be defined by the user.

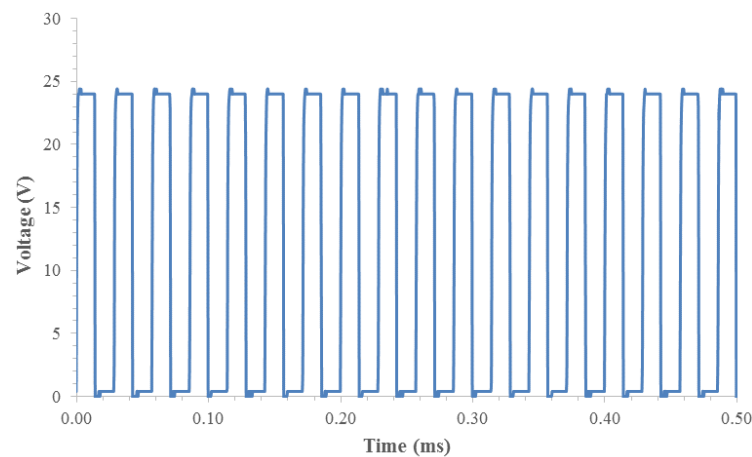


Figure 5. Sample pulse train from FPGA to input of servo amplifier.

2.3. Jet Production

As previously illustrated, the jet stagnation pressure emanating from a jet injector depends on a force balance between the driving force imparted on the plunger by the power source and the resistive force of pressure buildup in the chamber due to the bulk modulus of the working fluid, as well as any friction the device exhibits. This has been well-modeled by Baker and Sanders [9]. The equations are:

$$\frac{dp}{dt} = \frac{(B + p) \frac{dx}{dt} - \frac{BA_o}{A_p} \sqrt{\frac{2p}{\rho_o}}}{L - x_p}, \tag{1}$$

$$\frac{d^2x}{dt^2} = -\frac{F_p}{m_p} - \frac{A_p}{m_p} - \frac{dx}{dt} \frac{F_f}{m_p \left| \frac{dx}{dt} \right|}, \tag{2}$$

where B is the bulk modulus of the fluid, ρ_o is the initial density, p is the pressure and A_p and A_o are the piston and orifice area determined from the diameters of the piston and nozzle orifices, respectively. For water, $B = 2.18$ GPa and $\rho_o = 1000$ kg/m³ are used. x_p and dx/dt are the position and velocity of the piston, respectively, and $L = 80$ mm is the length of the liquid column inside the injector. m_p is the mass of the piston. F_p and F_f are the driving force and frictional force, respectively. For more details, see [9,25].

Utilizing a servo-controlled actuator makes it possible to decouple this set of ordinary differential equations, and therefore, it is no longer necessary to consider Equation (2), as the PID loops for position and velocity within the amplifier will ensure that it is possible to maintain any desired plunger velocity (dx/dt) to shape the pressure output of the device according to Equation (1). For a given velocity profile, the corresponding pressure and pressure changes can be easily obtained. The effects of changing friction due to O-ring friction or increased power demands for more viscous fluids no longer need to be considered. The errors caused by outside factors will be compensated at 8 kHz. Figure 6 illustrates the stagnation pressure behavior of the injector under a given velocity mapping with time.

The velocity map depicted in Figure 6 was tailored to yield a pressure pulse with a peak of 13 MPa and to have constant pressure output rather than a noticeable peak to show the controllability of the device and its ability to overcome the back-driving forces present within the injection chamber. The 13 MPa peak will illustrate the ability of the device to puncture human tissue, as it is at the upper limit of what is prescribed by Shergold et al. [55].

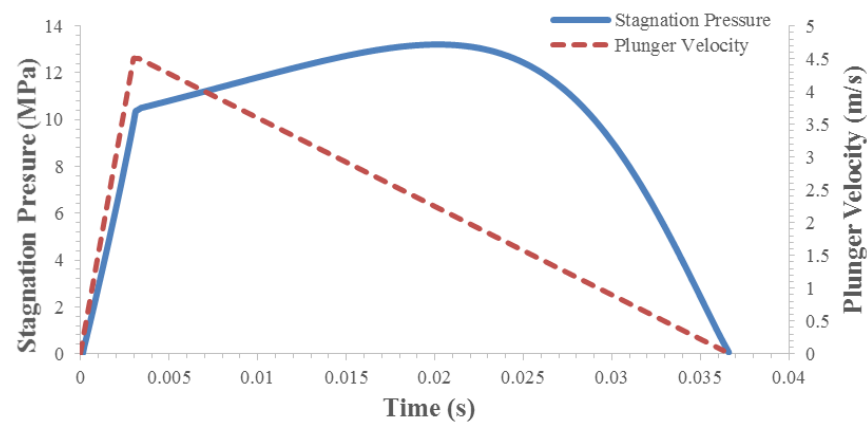


Figure 6. Pressure output as a function of theoretical plunger velocity.

2.4. Jet Pressure Measurement

The pressure traces in this particular study are captured through the use of a force transducer. The force measurements are then converted to pressures by utilizing the nozzle orifice area, given that there is negligible divergence at the standoff distances used to gather the data. Furthermore, the time frame of the phenomenon is such that the high response rate of piezoelectric sensors is required to properly map the pressure output. In this experiment, the 209C11 force transducer from PCB Piezotronics is used, with a measurement range of 9.8 N, a sensitivity of 494.60 mv/kN, and 0.5 Hz and 30 kHz for the lower and upper frequency response, respectively. The Force transducer is linked to a PCB Piezotronics ICP 482A22 signal conditioner, which is monitored by a Rigol DS1102E digital oscilloscope with 1 G Sa/s. The scope is triggered from the pulse stream sent by the FPGA to the servo amplifier; this aids in avoiding false triggers due to the noise generated by the power electronics of the servo amplifier. Furthermore, the force transducer is mounted on an aluminum-back plate, as is illustrated in Figure 7, which is secured to the testing apparatus via three magnets; this facilitates removal and ensures proper positioning of the sensor. The standoff distance used in the experiments corresponds to 0.8 mm, as it resulted in waveforms that were not affected by the overspray of the impinging jet.

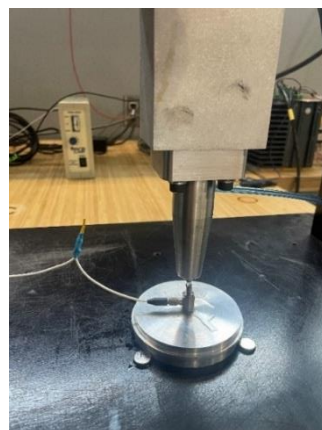


Figure 7. Close-up of force transducer and jet injector nozzle.

3. Results and Discussions

3.1. Validation of the Servo-Tube-Powered Injector for Stagnation Pressure Generation

In order to accurately demonstrate the feasibility of using permanent magnet synchronous linear motors as a power source for liquid jet injection, the ability to provide enough stagnation pressure and to penetrate human tissue was first examined. This needed to be accomplished without reaching the stalling current of the motor or excessively deviat-

ing in position-tracking error such that the servo loop could no longer recover. Although the power of a liquid jet can be modeled by

$$Power = \frac{1}{8}\pi\rho D^2 U^3, \quad (3)$$

where D is the diameter of the jet, and U is the jet velocity and yields a jet with a force of approximately 188 W, under the largest nozzle size (300 μm) and greatest density (1230 kg/m^3), far greater power is required to provide the impulse force necessary to pressurize the chamber for proper liquid jet formation. According to the plunger velocity map depicted in Figure 6, a theoretical power of 9.1 kW was required. This lies below the 13 kW the Compax3 can provide and was the threshold for the peak injection pressures.

The first set of data illustrates the ability of the servo-driven injector to produce a pressure output great enough to puncture tissue. For this experiment, a pressure curve with an average stagnation pressure of 13 MPa was desired, and the corresponding velocity profile illustrated in Figure 6 mentioned above was programmed into the FPGA.

Figure 8 depicts an overlay of the experimental trace to the desired pressure output of the device. The initial pressure spike oscillated about the desired values as the desired output climbed to 10 MPa, and the experimental trace then overshoot by approximately 3 MPa, at which point the velocity of the plunger began to decrease and the PID could begin to diminish the error. The overshoot in this situation represents 30% of the target value. Improving the error could be accomplished by increasing the response time of the servo loop; however, there are a few factors that limited what could be achieved with this amplifier. The first was the control frequency of the PID loop, which was set to 8 kHz; ideally this should be on the order of 30 kHz, in order to respond faster than the transmission of the pressure wave in the injection chamber. In the current experimental setup, the switching frequency was also limited by the maximum switching frequency of the IGBTs and the ability to energize the motor windings with the appropriate amplitude and frequency AC current.

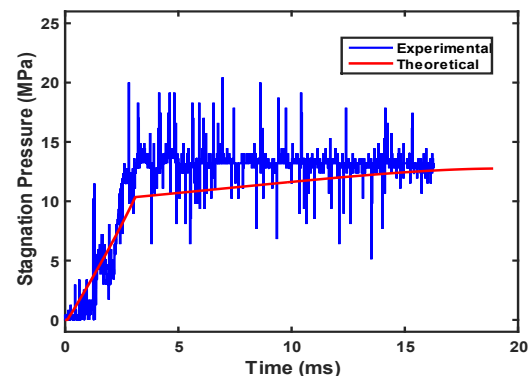


Figure 8. Experimental and theoretical overlay of stagnation pressure for initial velocity profile.

Nevertheless, it was observed from Figure 9 that the traces remained consistent over repeated trials, thus concluding that the device seems to display an acceptable level of repeatability. Moreover, a high-speed photo sequence of the jet, taken penetrating 10% ballistic gel with the use of a pco.1200 hs high-speed digital CMOS camera (PCO GmbH), illustrated that the injector could penetrate human tissue and overcome the initial forces required to produce a high-speed pressure pulse; see Figure 10.

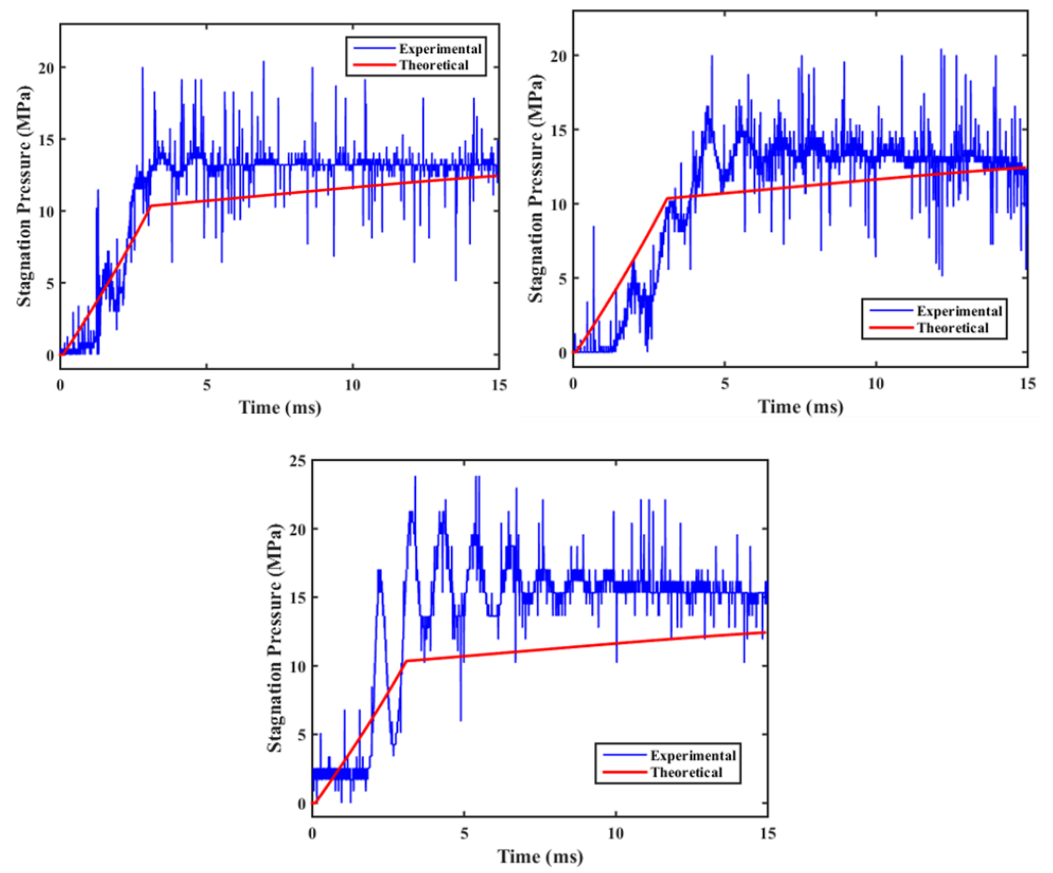


Figure 9. Test trials illustrating repeatability of servo-tube injector in shaping pressure pulse.

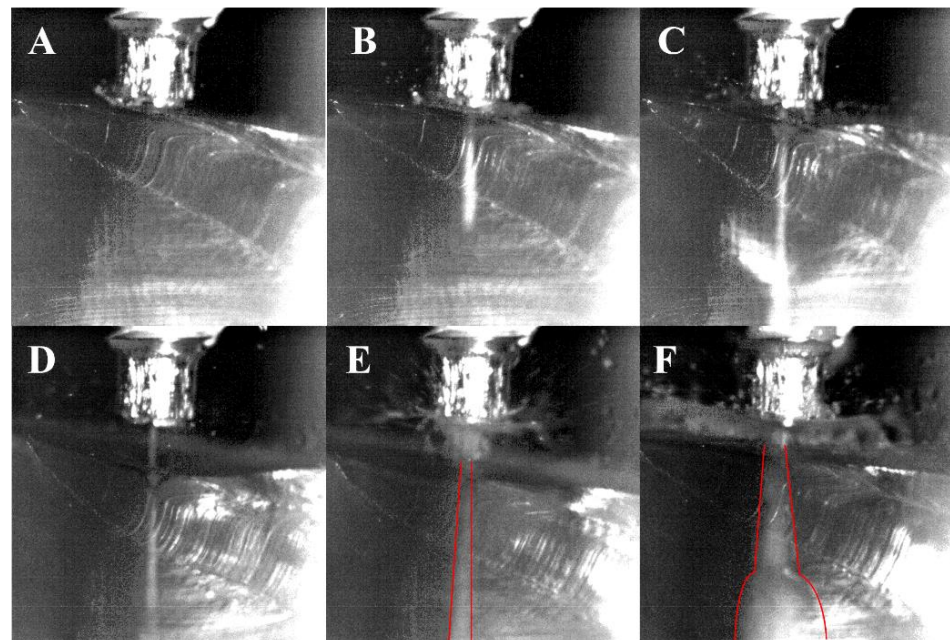


Figure 10. High-speed sequence of servo-tube injector penetrating 10% ballistic gel. (A–F) shows the injection snapshots at increasing time sequence.

Although the pressure waveform that was programmed into the device did not display a typical peak followed by an average stagnation pressure, it penetrated the ballistic gel cleanly upon initial contact. It was possible to observe the typical traits of a high-speed liquid jet injection as the jet penetrates the gel. The liquid jet reached a target depth and

then began to deposit more fluid at this depth, whereby a bulbus was seen forming. It should also be noted that the backsplash observed in Figure 10 was due to the fact that ballistic gel does not absorb liquid as tissue does, as described by Shergold et al. [55]; hole formation was due to a crack propagation through the gel, and as the injection made its way to the end, the crack closed, forcing the liquid to the surface.

3.2. Reproducing Standard Injector Performance

One of the key elements in illustrating the prototype's feasibility is the ability to shape a pressure output and consistently maintain that result with respect to changing nozzle size and fluid viscosity. Therefore, it was decided to reproduce a similar pressure output in line with commercially available units. Figure 11 depicts a stagnation pressure wave, with a peak of 15 MPa occurring at 5 ms and an average delivery pressure of 6 MPa reached at approximately 7.5 ms and utilizing the servo amplifier's maximum rates of accel/decel.

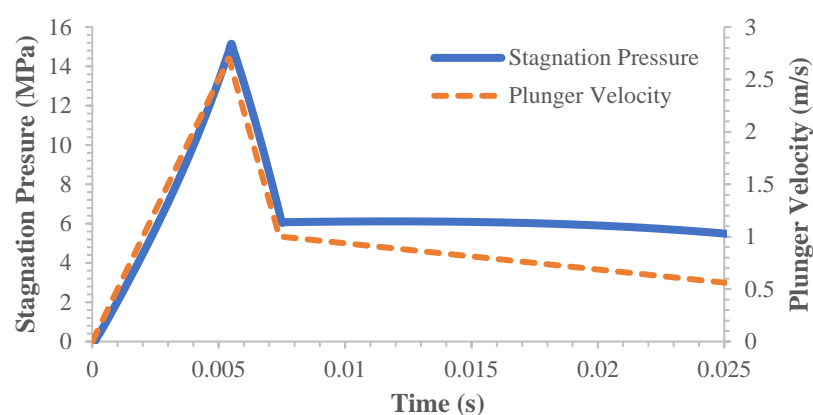


Figure 11. Pressure Profile representing typical behavior of commercially available injectors.

This velocity profile was tested under seven different viscosities and four different nozzle sizes. The fluid viscosity was varied by utilizing glycerol and making aqueous solutions of different weight percentages. Figure 12 shows the variation of both density and viscosity as a function of weight %; the different test conditions correspond to 0, 20, 30, 40, 60, 70 and 80 wt.% glycerol, respectively. Each nozzle size and viscosity combination were run with a minimum of 12 repetitions to ensure meaningful conclusions could be drawn from the data sets. It should also be noted that 90 and 100 wt.% were also considered, as the test device could create a liquid jet without attaining the stalling current of the linear motor; however, after approximately three injections, the nozzles would show signs of blockage. It was impossible to dislodge the blockage without heating the tip of the nozzle with a propane torch, which would cause deformation of the orifice. Consequently, it was decided to test only up to 80 wt.% in order to extend the longevity of the nozzles.

Figure 13 depicts an initial pressure trace, which illustrates the system's ability to dynamically shape a pressure profile. One of the positive aspects of the gathered results shows that the system accurately reached the desired peak and mean injection pressures. Discrepancies were found in the time required to reach the peak, which was targeted at 5 ms, but occurred at approximately 2.5 ms, a trend that is consistent with all the profiles that were tested; further investigation into this phenomenon needs to be conducted. Oscillations about the mean injection pressure were also observed; this is in line with pressure plots from other needle-free devices. Although the oscillations were present, they settled toward the tail end of the injection. The oscillation can partly be attributed to the rapid loading and unloading of the piezoelectric force sensor.

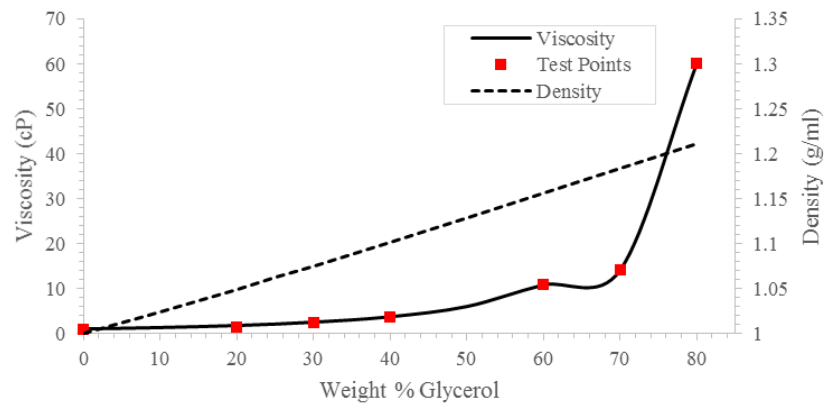


Figure 12. Density and viscosity as a function of weight % glycerol.

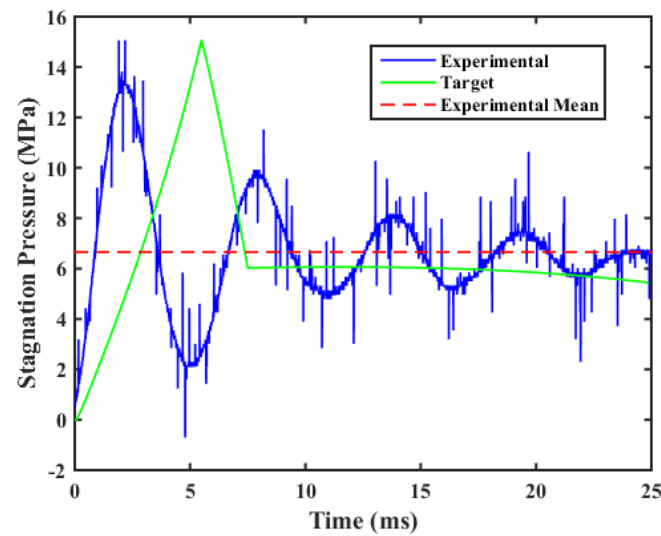


Figure 13. A sample showing the experimental and target pressure profile to illustrate the system’s ability to dynamically shape a pressure profile.

Comparisons between the experimental values displayed in Figure 14 and the theoretical values, corrected for change in density of the fluid and nozzle size, yielded maximum deviations of approximately 5.5 MPa when comparing pressure peaks and 1.37 MPa when comparing mean stagnation pressures.

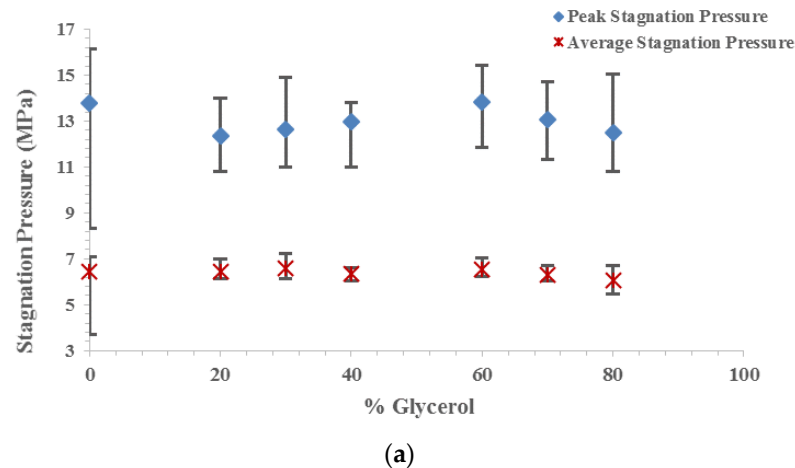
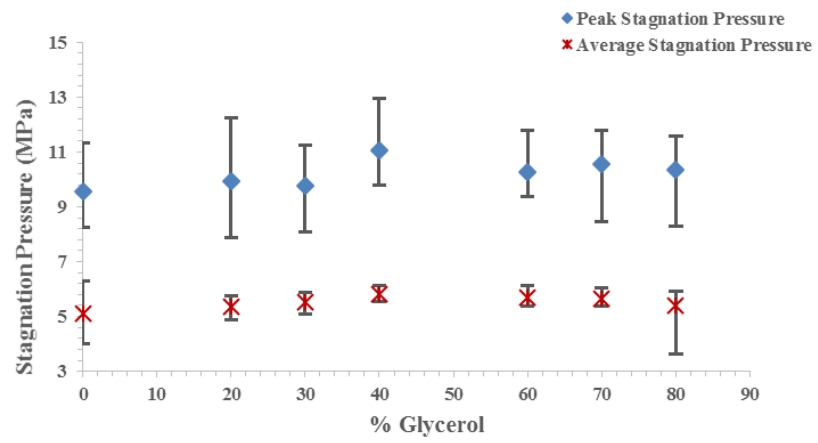
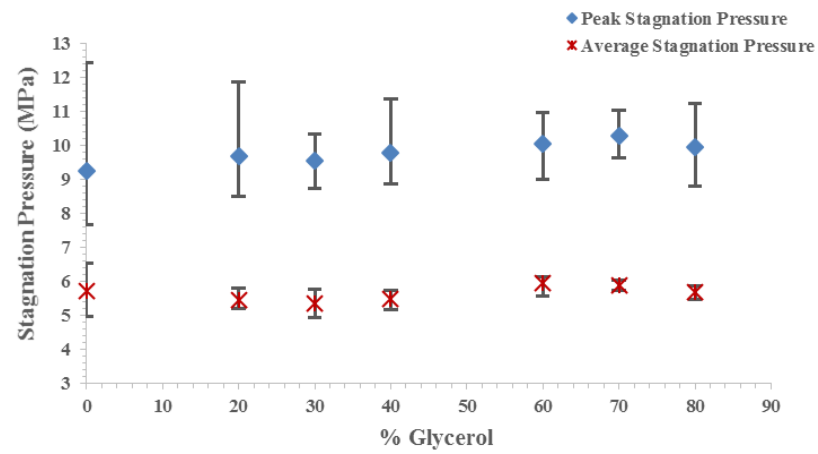


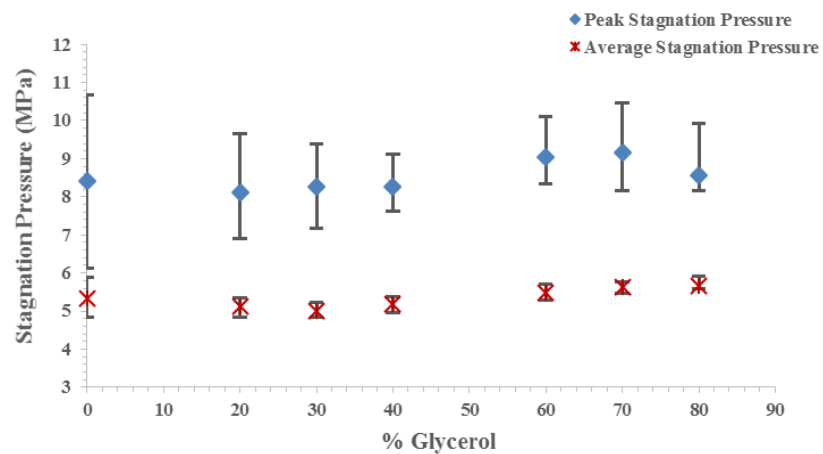
Figure 14. Cont.



(b)



(c)



(d)

Figure 14. Experimental and targeted pressure profiles tested under various viscosities and nozzle sizes: (a) Nozzle 6, (b) 8, (c) 10 and (d) 12.

3.3. Pressure Profile Shaping for Large-Volume Injection

The device was also verified for its ability to produce large-volume, pulsed injections. It is hypothesized that this technique can offer additional benefits as it will not overload the tissue with one large dose but deliver it in a gradual manner. This aids in increasing injection completeness as well as the accuracy of targeted tissue depth. Figure 15 illustrates the injector delivering a two-pulse injection with the first phase at 15 MPa and the second phase at 7.5 MPa, corresponding to half the pulse frequency of the first but on the same interval duration.

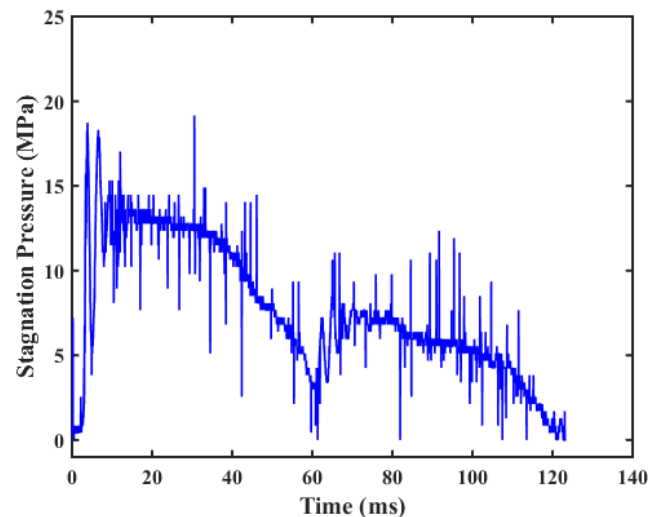


Figure 15. The stagnation pressure evolution for a two-pulse injection profile.

Figure 16 illustrates the system's ability to deliver an injection corresponding to an injection volume of approximately 0.2 mL per pulse. In order to obtain the pulsing action, a delay of 50 ms was added in between each pulse, and the pulse magnitude, as well as the duration, remained consistent throughout the multiple profiles. Hence, the pulsed injections were delivered at a frequency of approximately 10 Hz. The chamber was filled once to its complete volume at the beginning of the pulse sequence, and therefore, the subsequent pulsed jets constituted a fraction of the total chamber volume; consequently, the jet behavior was shown the same for each pulse.

The device exhibited a good level of repeatability, attaining a mean pressure of 13 MPa per pulse. Further investigation is necessary to determine the maximum frequency at which the pulses can be delivered without blending; in the current study, a gap of 30 ms was the minimum that could be used in order to see two distinct peaks. Moreover, the accuracy of the pulse length will also depend on the precision and speed displayed by the control loop and linear motor combination.

Overall, the device appeared to perform well in shaping a pressure profile, with very repeatable average stagnation pressures. The peak pressures displayed greater variation, and future studies should focus on quantifying the effect of servo response time vs. fluid response. This can be achieved by building a custom amplifier that not only makes use of high-power-high-frequency IGBTs and control hardware capable of working on the order of MHz, but also considers the real-time pressure output in order to build a feed-forward model for the device so that it can be used more accurately.

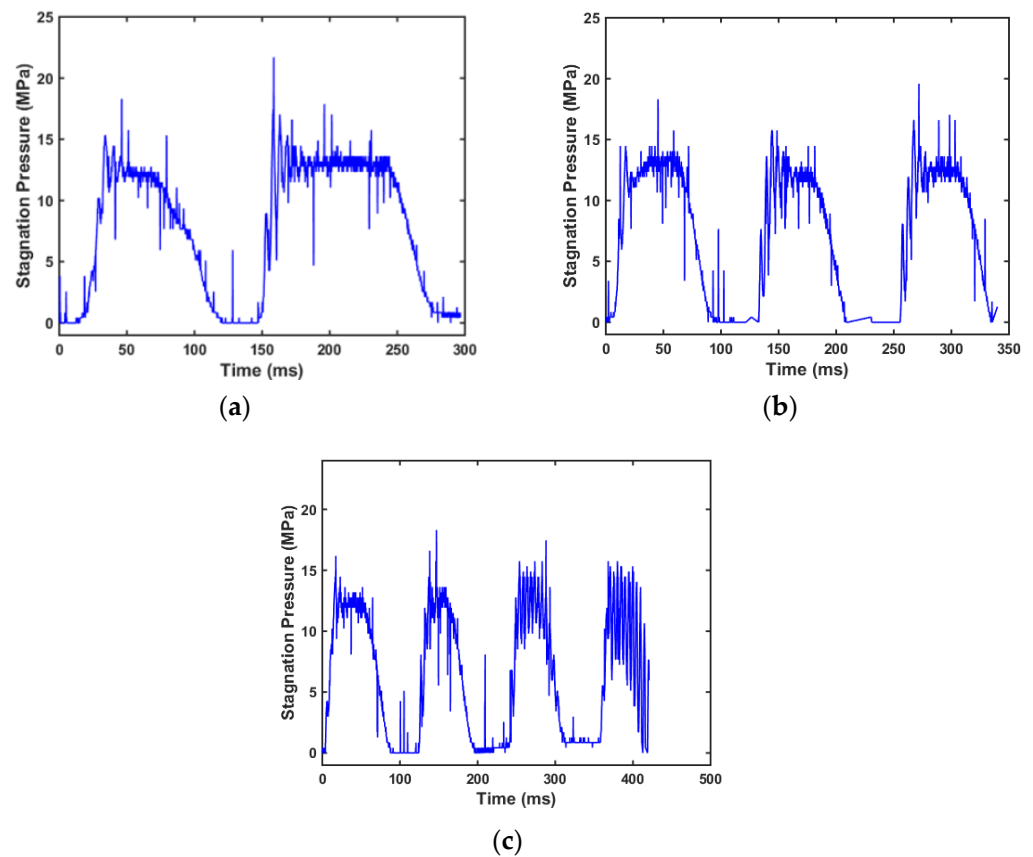


Figure 16. Results showing the capability of the present prototype to shape the pressure profile and deliver different multiple pulse injections: (a) two pulses, (b) three pulses and (c) four pulses. The pulsed injections in each case were delivered at a frequency of approximately 10 Hz, and each pulse was approximately 0.2 mL of injectate.

3.4. Penetration of the Liquid Jet Produced by the Present Prototype


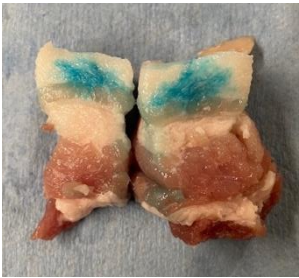
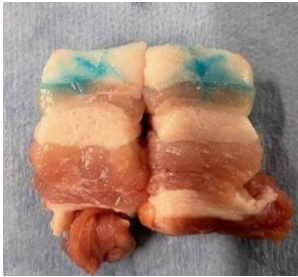

It was also possible to examine the device's ability to penetrate and deposit medication in real tissue. This short series of tests made it possible to verify whether different targets could be attained by utilizing two different pressure curves, water as a test fluid and a 150 μm nozzle. The volume chosen for the initial penetration study was 0.4 mL, which corresponds to 10 mm of downward travel. In order to ensure the proper volume of fluid was delivered for each sample, the chamber was filled and then primed once; at that point, the sample was placed underneath, and the injection was performed. Test samples of 40 mm to 45 mm thick pig thigh, obtained from the consumer market, weighing from 26 g to 35 g, were created and brought to room temperature. The samples were then placed, as illustrated in Figure 17, under the injector, utilizing a spacer to compress the samples up against the orifice so there would be no standoff distance. The first set of tests looked at the injector's ability to achieve different depths with the outer skin removed, as the tensile strength of pork skin increases as the tissue dries.



Figure 17. Close-up of porcine tissue and jet injector nozzle.

The penetration of the pork tissue delivered promising results; the two different profiles were able to deposit at different depths. Furthermore, the samples were weighed pre- and post-injection to determine the level of completeness. In Table 6, the pre-injection and post-injection weights were obtained using an OHAUS Scout SPX421. The pre-injection weight for the profile corresponded to 31.7 g and post-injection at 32.1 g, indicating a delivery efficiency of 100%. However, it should be noted that the weight of the sample could only be obtained within 0.1 g; thus, a more accurate scale should reveal a delivery efficiency of less than 100%. These numbers should be used to give a general behavior of delivery efficiency, and more detailed penetration studies that quantify the effect of backslash should be conducted.

Table 6. Penetration Test (Porcine Tissue).

Profile	Initial View	Dissected View
Test 1 (15 MPa injection)		
Test 2 (7.5 MPa injection)		

It is worth noting that, due to the current experimental limitation and facility constraints, the results in Table 6 for two pressure profiles are provided mainly for illustration purposes to demonstrate the injection capability of the present prototype. A more systematic investigation of the present needle-free jet injector prototype in a well-controlled porcine tissue model, similar to the study by Ruddy et al. [56], is required in future work.

4. Concluding Remarks

The prototype injector created in this study shows promising potential. It can shape a pressure profile in real time, deliver large-volume injections in single or pulsating modes and create the necessary force required for needle-free drug delivery. Future studies can now focus on developing power electronics that can operate at faster speeds to help improve the accuracy of the device, as well as scaling down the size of the actuator, reducing its inertia and further improving response times and usability. This prototype can also be used to provide researchers with a platform on which to study the effects of different pressure profiles on injection depth and completeness. Nevertheless, it should be noted that there are limitations to the maximum peak pressures that can practically be achieved utilizing linear actuators. The pressure profiles provided in this study were generated utilizing the maximum current capacity of the servo amplifier, and although the actuators themselves can handle a very large amount of inrush current, even as they are scaled down in size, the amplifier drives will require larger power electronics, which may not be ideal for a clinical setting. Consequently, research should not be limited to electronically controlled injectors, but should also focus on developing and characterizing power sources that can deliver high-power output with less complexity, such as is the case in [54], which deals with combustion-driven, needle-free injectors.

Author Contributions: Conceptualization, R.P. and H.D.N.; methodology, R.P.; investigation, R.P.; formal analysis, R.P. and H.D.N.; writing—original draft preparation, R.P.; writing—review and editing, R.P. and H.D.N. All authors have read and agreed to the published version of the manuscript.

Funding: This work was supported by the Natural Sciences and Engineering Research of Canada NSERC (No. RGPIN-2017-06698).

Institutional Review Board Statement: Not applicable.

Informed Consent Statement: Not applicable.

Data Availability Statement: Not applicable.

Conflicts of Interest: The authors declare no conflict of interest.

References

1. Mitragotri, S. Current status and future prospects of needle free liquid jet injectors. *Nat. Rev. Drug Discov.* **2006**, *5*, 543–548. [[CrossRef](#)] [[PubMed](#)]
2. Baxter, J.; Mitragotri, S. Needle-free liquid jet injections: Mechanisms and applications. *Expert Rev. Med. Devices* **2006**, *3*, 565–574. [[CrossRef](#)]
3. Mohizin, A.; Kim, J.K. Current engineering and clinical aspects of needle-free injectors: A review. *J. Mech. Sci. Technol.* **2018**, *32*, 5737–5747. [[CrossRef](#)]
4. Ravi, A.D.; Sadhna, D.; Nagpaal, D.; Chawla, L. Needle free injection technology: A complete insight. *Int. J. Pharm. Investig.* **2015**, *5*, 192–199. [[CrossRef](#)] [[PubMed](#)]
5. Barolet, D.; Benohanian, A. Current trends in needle-free jet injection: An update. *Clin. Cosmet. Investig. Dermatol.* **2018**, *11*, 231–238. [[CrossRef](#)] [[PubMed](#)]
6. Vadlapatla, R.; Gayakwad, S.; Yellepeddi, V.; Wong, E.Y. Needle-free injectors. In *Drug Delivery Devices and Therapeutic Systems*, 1st ed.; Chappel, E., Ed.; Academic Press: London, UK, 2021; pp. 199–211.
7. Han, H.S.; Hong, J.Y.; Kwon, T.R.; Lee, S.E.; Yoo, K.H.; Choi, S.Y.; Kim, B.J. Mechanism and clinical applications of needle-free injectors in dermatology: Literature review. *J. Cosmet. Dermatol.* **2021**, *20*, 3793–3801. [[CrossRef](#)]
8. Wang, R.; Bian, Q.; Xu, Y.; Xu, D.; Gao, J. Recent advances in mechanical force-assisted transdermal delivery of macromolecular drugs. *Int. J. Pharm.* **2021**, *602*, 120598. [[CrossRef](#)] [[PubMed](#)]
9. Baker, A.B.; Sanders, J.E. Fluid mechanics analysis of a spring-loaded jet injector. *IEEE Trans. Biomed. Eng.* **1999**, *46*, 235–242. [[CrossRef](#)]
10. Schramm, J.R.; Mitragotri, S. Transdermal drug delivery by jet injectors: Energetics of jet formation and penetration. *Pharm. Res.* **2002**, *19*, 1673–1679. [[CrossRef](#)]
11. Schramm-Baxter, J.; Mitragotri, S. Needle-free jet injections: Dependence of jet penetration and dispersion in the skin on jet power. *J. Control. Release* **2004**, *97*, 527–535. [[CrossRef](#)]
12. Baxter, J.; Mitragotri, S. Jet-induced skin puncture and its impact on needle-free jet injections: Experimental studies and a predictive model. *J. Control. Release* **2005**, *106*, 361–373. [[CrossRef](#)] [[PubMed](#)]

13. Brown, M.B.; Martin, G.P.; Jones, S.A.; Akomeah, F.K. Dermal and transdermal drug delivery systems: Current and future prospects. *Drug Deliv.* **2006**, *13*, 175–187. [[CrossRef](#)] [[PubMed](#)]
14. Chen, K.; Zhou, H.; Li, J.; Cheng, G.J. A model on liquid penetration into soft material with application to needle-free jet injection. *ASME J. Biomech. Eng.* **2010**, *132*, 101005. [[CrossRef](#)] [[PubMed](#)]
15. Chen, K.; Zhou, H.; Li, J.; Cheng, G. Stagnation pressure in liquid needle-free injection: Modeling and experimental validation. *J. Drug Deliv. Lett.* **2011**, *1*, 97–104.
16. Schneider, A.; Mueller, P.; Jordi, C.; Richard, P.; Sneeringer, P.; Nayyar, R.; Yovanoff, M.; Lange, J. Hold the device against the skin: The impact of injection duration on user's force for handheld autoinjectors. *Expert Opin. Drug Deliv.* **2020**, *17*, 225–236. [[CrossRef](#)]
17. Mohizin, A.; Kim, J.K. Dispersion profile of a needle-free jet injection depends on the interfacial property of the medium. *Drug Deliv. Trans. Res.* **2022**, *12*, 384–394. [[CrossRef](#)] [[PubMed](#)]
18. Rohilla, P.; Marston, J.O. In-vitro studies of jet injections. *Int. J. Pharm.* **2019**, *568*, 118503. [[CrossRef](#)]
19. Rane, Y.S.; Marston, J.O. Transient modelling of impact driven needle-free injectors. *Comput. Biol. Med.* **2021**, *135*, 104586. [[CrossRef](#)]
20. Mohanty, C.; Mannavathy, C.; Srikanth, D.; Tabassum, R. Needle free drug delivery systems: A review. *Int. J. Pharm. Res. Dev.* **2011**, *3*, 7–15.
21. Mohizin, A.; Lee, D.; Kim, J.K. Impact of the mechanical properties of penetrated media on the injection characteristics of needle-free jet injection. *Exp. Therm. Fluid Sci.* **2021**, *126*, 110396. [[CrossRef](#)]
22. Mohizin, A.; Kim, J.K. Effect of geometrical parameters on the fluid dynamics of air-powered needle-free jet injectors. *Comput. Biol. Med.* **2020**, *118*, 103642. [[CrossRef](#)] [[PubMed](#)]
23. Shapiro, J.R.; Hodgins, B.; Hendin, H.E.; Patel, A.; Menassa, K.; Menassa, C.; Menassa, M.; Pereira, J.A.; Ward, B.J. Needle-free delivery of influenza vaccine using the Med-Jet[®] H4 is efficient and elicits the same humoral and cellular responses as standard IM injection: A randomized trial. *Vaccine* **2019**, *37*, 1332–1339. [[CrossRef](#)] [[PubMed](#)]
24. Zeng, D.; Wu, N.; Qian, L.; Shi, H.; Kang, Y. A novel controllable pneumatic needle-free injection system for large-volume drug delivery. *J. Pharm. Sci.* **2020**, *109*, 1772–1779. [[CrossRef](#)] [[PubMed](#)]
25. Portaro, R.; Ng, H.D. Experiments and modeling of air-powered needle free liquid injectors. *J. Med. Biol. Eng.* **2015**, *35*, 685–695. [[CrossRef](#)]
26. Nakayama, H.; Portaro, R.; Kiyanda, C.B.; Ng, H.D. CFD modeling and validation of high-speed liquid jets from an air-powered needle-free injection system. *J. Mech. Med. Biol.* **2015**, *16*, 1650045. [[CrossRef](#)]
27. Kim, J.K.; Mohizin, A.; Lee, S.K. Experimental investigation on key parameters in air-powered needle-free injection system for skin treatment. *J. Korean Soc. Vis.* **2018**, *16*, 42–47.
28. Trimzi, M.A.; Ham, Y.B. A needle-free jet injection system for controlled release and repeated biopharmaceutical delivery. *Pharmaceutics* **2021**, *13*, 1770. [[CrossRef](#)]
29. Arora, A.; Hakim, I.; Baxter, J.; Rathnasingham, R.; Srinivasan, R.; Mitragotri, S. Needle free delivery of macromolecules across the skin by nanolitre-volume pulsed microjets. *Proc. Nat. Acad. Sci. USA* **2007**, *104*, 4255–4260. [[CrossRef](#)]
30. Stachowiak, J.C.; von Muhlen, M.G.; Li, T.H. Piezoelectric control of needle free transdermal drug delivery. *J. Control. Release* **2007**, *124*, 88–97. [[CrossRef](#)]
31. Menezes, V.; Nakagawa, A.; Takayama, K. Laser-based pulsed liquid microjet for surgery. *J. Indian Inst. Sci.* **2006**, *86*, 207–214.
32. Tagawa, Y.; Oudalov, N.; Visser, C.W.; Peters, I.R.; van der Meer, D.; Sun, C.; Prosperetti, A.; Lohse, D. Highly focused supersonic microjets. *Phys. Rev. X* **2012**, *2*, 031002. [[CrossRef](#)]
33. Lee, J.J.; Yi, K.H.; Kim, H.S.; An, M.H.; Seo, K.K.; Huh, C.H.; Kim, H.J. A novel needle-free microjet drug injector using Er: YAG laser: A completely new concept of transdermal drug delivery system. *Clin. Anat.* **2022**, *35*, 682–685. [[CrossRef](#)]
34. Kiyama, A.; Endo, N.; Kawamoto, S.; Katsuta, C.; Oida, K.; Tanaka, A.; Tagawa, Y. Visualization of penetration of a high-speed focused microjet into gel and animal skin. *J. Vis.* **2019**, *22*, 449–457. [[CrossRef](#)]
35. Schoppink, J.; Fernandez Rivas, D. Jet injectors: Perspectives for small volume delivery with lasers. *Adv. Drug Deliv. Rev.* **2022**, *182*, 114109. [[CrossRef](#)] [[PubMed](#)]
36. Krizek, J.; De Goumoëns, F.; Delrot, P.; Moser, C. Needle-free delivery of fluids from compact laser-based jet injector. *Lab Chip* **2020**, *20*, 3784. [[CrossRef](#)] [[PubMed](#)]
37. Miyazaki, Y.; Usawa, M.; Kawai, S.; Yee, J.; Muto, M.; Tagawa, Y. Dynamic mechanical interaction between injection liquid and human tissue simulat induced by needle-free injection of a highly focused microjet. *Sci. Rep.* **2021**, *11*, 14544. [[CrossRef](#)]
38. Fletcher, D.A.; Palanker, D.V. Pulsed liquid microjet for microsurgery. *Appl. Phys. Lett.* **2001**, *78*, 1933–1935. [[CrossRef](#)]
39. Miyazaki, H.; Atobe, S.; Suzuki, T.; Iga, H.; Terai, K. Development of pyro-drive jet injector with controlled jet pressure. *J. Pharm. Sci.* **2019**, *108*, 2415–2420. [[CrossRef](#)]
40. Taberner, A.; Hogan, N.C.; Hunter, I.W. Needle-free jet injection using real-time controlled linear Lorentz-force actuators. *Med. Eng. Phys.* **2012**, *34*, 1228–1235. [[CrossRef](#)]
41. Li, X.; Ruddy, B.; Taberner, A. Characterization of needle-assisted jet injections. *J. Control. Release* **2016**, *243*, 195–203. [[CrossRef](#)]
42. Williams, R.M.J.; Ruddy, B.P.; Hogan, N.C.; Hunter, I.W.; Nielsen, P.M.F.; Taberner, A.J. Analysis of moving-coil actuator jet injectors for viscous fluids. *IEEE Trans. Biomed. Eng.* **2016**, *63*, 1099–1106. [[CrossRef](#)]
43. Ruddy, B.P.; Dixon, A.W.; Williams, R.M.J.; Taberner, A.J. Optimization of portable electronically-controlled needle-free jet injection systems. *IEEE/ASME Trans. Mechatron.* **2017**, *22*, 2013–2021. [[CrossRef](#)]

44. McKeage, J.W.; Ruddy, B.P.; Nielsen, P.M.F.; Taberner, A.J. The effect of jet speed on large volume jet injection. *J. Control. Release* **2018**, *280*, 51–57. [[CrossRef](#)] [[PubMed](#)]
45. Brennan, K.A.; Ruddy, B.P.; Nielsen, P.M.F.; Taberner, A.J. Classification of diffuse light emission profiles for distinguishing skin layer penetration of a needle-free jet injection. *Biomed. Opt. Express* **2019**, *10*, 5081–5092. [[CrossRef](#)] [[PubMed](#)]
46. Kojic, N.; Goyal, P.; Lou, C.H.; Corwin, M.J. An innovative needle-free injection system: Comparison to 1 ml standard subcutaneous injection. *AAPS PharmSciTech* **2017**, *18*, 2965–2970. [[CrossRef](#)]
47. Kelley, E.L.; Smith, R.H.; Corcoran, G.; Nygren, S.; Jacoski, M.V.; Fernandes, A. Advances in subcutaneous injections: PRECISE II: A study of safety and subject preference for an innovative needle-free injection system. *Drug Deliv.* **2021**, *28*, 1915–1922. [[CrossRef](#)]
48. Raviprakash, K.; Porter, K.R. Needle-free injection of DNA vaccines: A brief overview and methodology. *Methods. Mol. Med.* **2006**, *127*, 83–89.
49. Kendall, M. Engineering of needle-free physical methods to target epidermal cells for DNA vaccination. *Vaccine* **2006**, *24*, 4651–4656. [[CrossRef](#)]
50. Portaro, R.; Ng, H.D. Analysis of High-Speed Jets Produced by a Servo Tube Driven Liquid Jet Injector. In Proceedings of the 70th Annual Meeting of the APS Division of Fluid Dynamics, Denver, CO, USA, 19–21 November 2017.
51. Do, N.N.L.; Taberner, A.J.; Ruddy, B.P. Design of a Linear Permanent Magnet Synchronous Motor for Needle-free Jet Injection. In Proceedings of the 2017 IEEE Energy Conversion Congress and Exposition (ECCE), Cincinnati, OH, USA, 1–5 October 2017.
52. Do, N.N.L.; Taberner, A.J.; Ruddy, B.P. A linear permanent magnet synchronous motor for large volume needle-free jet injection. *IEEE Trans. Ind. Appl.* **2018**, *55*, 1437–1446. [[CrossRef](#)]
53. Aerotech. Linear Motors: Application Guide. Available online: www.aerotech.com (accessed on 1 May 2022).
54. Portaro, R.; Sadek, J.; Xu, H.; Ng, H.D. Controlled release using gas detonation in needle-free liquid jet injections for drug delivery. *Appl. Sci.* **2019**, *9*, 2712. [[CrossRef](#)]
55. Shergold, O.A.; Fleck, N.A. Mechanisms of deep penetration of soft solids, with application to the injection and wounding of skin. *Proc. R. Soc. Lond. A* **2004**, *460*, 3037–3058. [[CrossRef](#)]
56. Ruddy, B.P.; Bullen, C.; Ting, J.W.C.; Jeong, S.H.; Madadkhahsalmassi, B.; McKeage, J.W.; Svirskis, D.; Tingle, M.D.; Xu, J.; Taberner, A.J. Subcutaneous nicotine delivery via needle-free jet injection: A porcine model. *J. Control. Release* **2019**, *306*, 83–88. [[CrossRef](#)] [[PubMed](#)]